Article

Additivity of Atomic Strain Fields as a Tool to Strain-Engineering Phase-Stabilized CsPbI$_3$ Perovskites

Johannes L. Teunissen,* Tom Braeckevelt, Irina Skvortsova, Jinhui Guo, Bapi Pradhan, Elke Debroye, Maarten B. J. Roeffaers, Johan Hofkens, Sandra Van Aert, Sara Bals, Sven M. J. Rogge, and Veronique Van Speybroeck*

Read Online

ACCESS | 📊 Metrics & More | 📖 Article Recommendations | 🆂🅸 Supporting Information

ABSTRACT: CsPbI$_3$ is a promising perovskite material for photovoltaic applications in its photoactive perovskite or black phase. However, the material degrades to a photovoltaically inactive or yellow phase at room temperature. Various mitigation strategies are currently being developed to increase the lifetime of the black phase, many of which rely on inducing strains in the material that hinder the black-to-yellow phase transition. Physical insight into how these strategies exactly induce strain as well as knowledge of the spatial extent over which these strains impact the material is crucial to optimize these approaches but is still lacking. Herein, we combine machine learning potential-based molecular dynamics simulations with our in silico strain engineering approach

to accurately quantify strained large-scale atomic structures on a nanosecond time scale. To this end, we first model the strain fields introduced by atomic substitutions as they form the most elementary strain sources. We demonstrate that the magnitude of the induced strain fields decays exponentially with the distance from the strain source, following a decay rate that is largely independent of the specific substitution. Second, we show that the total strain field induced by multiple strain sources can be predicted to an excellent approximation by summing the strain fields of each individual source. Finally, through a case study, we illustrate how this additive character allows us to explain how complex strain fields, induced by spatially extended strain sources, can be predicted by adequately combining the strain fields caused by local strain sources. Hence, the strain additivity proposed here can be adopted to further our insight into the complex strain behavior in perovskites and to design strain from the atomic level onward to enhance their sought-after phase stability.
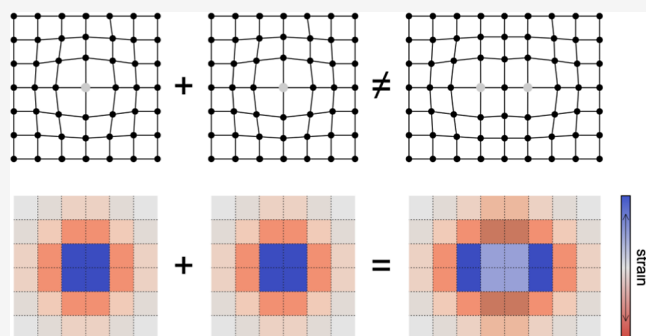
1. INTRODUCTION

Perovskites are promising materials for photovoltaic applications.[1] However, hybrid organic–inorganic perovskites, which currently show the highest power conversion efficiencies, suffer from short device lifetimes due to the volatility of the organic cations.[2,3] Substituting the organic cations with cesium ions may elongate the device lifetime, thus obtaining more stable[4] purely inorganic metal halide perovskites (MHPs) such as CsPbI$_3$, with devices currently reaching a photovoltaic efficiency of up to 25%.[5] Yet, CsPbI$_3$ suffers from a phase stability problem at ambient conditions, with the yellow photoinactive phase being more stable than the black perovskite phase under these conditions.[6] As the yellow phase has a smaller volume, the black-to-yellow transition induces an abrupt and highly anisotropic volume contraction.[7,8] Various strategies are known to stabilize the black CsPbI$_3$ phase,[9,10] such as reducing the perovskite grain size,[7] resulting in nanocrystals[11] or thin films[12] that can be obtained through surface passivation[13] or confinement within porous materials.[14] However, stabilization can also be achieved via partial ion substitution, either through

electron doping[9] or other defect-engineering techniques.[15] An example of the structural fragment of CsPbI$_3$ with a single ion substitution acting as a defect is shown in Figure 1. These latter approaches fit the observation that well-chosen strains can substantially increase the black phase stability. Such strain can be experimentally introduced through, for instance, pressure,[16] partial substitution with larger organic cations,[17] or biaxial strain induced by substrate clamping.[18] For CsPbI$_3$ nanocrystals, dopant concentrations of about 10% succeed in stabilizing the black phase,[19,20] and a lower concentration of about 5% is sufficient to obtain the same goal in perovskite thin films given the additional interfacial strain induced due to the mismatch between the thin film and the substrate.[21]
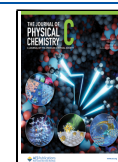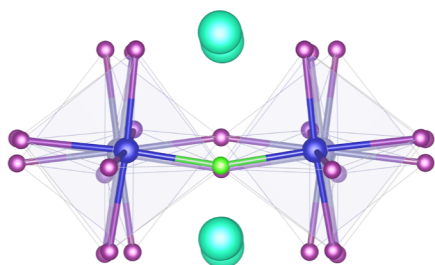
Figure 1. Exemplary fragment of CsPbI$_3$ with a single I → Cl substitution. Color code: lead (blue, including semitransparent polyhedra), iodine (purple), chlorine (lime), and cesium (cyan).

While all these different strain sources lead, to a certain extent, to black phase stabilization, the magnitude of the strain they induce in the material and the spatial range over which these structural alterations impact the material remain largely unknown. Yet, such physical insight is crucial to determine which strains are necessary in a given material to phase stabilize the black phase while minimally affecting the other, attractive material properties, as well as to pinpoint which strain sources are best suited to realize the required phase-stabilizing strains from the atomic level onward. Due to the lack of such an overarching metric to quantify strain from the atom to the material level, current strain stabilization approaches mainly focus on introducing a structural mismatch between the material's different constituents, for example, quantified by the Goldschmidt tolerance factor.[22] However, it has become clear that tolerance factors, based merely on atomic radii, are insufficient to describe dynamic strain effects.[23] For instance, they cannot explain how the same phase stabilization effect is reached by building blocks that are either too large or too small.[24,25] In this work, we aim to overcome this fundamental drawback and illustrate how strain engineering forms an overarching approach to causally correlate how different strain

sources induce strain in a material and how this strain eventually alters the phase stability and macroscopic material response.

Although the exact black-to-yellow transition mechanism in CsPbI$_3$ is still unknown, it is generally expected that the transition initiates when the PbI$_6^{4-}$ octahedra start to tilt, such that adjacent octahedra become edge-sharing instead of corner-sharing.[26,27] Besides the octahedral tilting, the rattling of the cesium atoms also contributes to the phase instability.[25] The phase transition is described as nonmartensitic, meaning that the transition occurs along an amorphous interface.[28] These observations are supported by the loss of all substrate clamping during the transition.[18] Hence, it is clear that while the black-to-yellow phase transformation affects the macroscopic material response, it originates from local deviations from the equilibrium black structure. As a result, any overarching stabilization approach must be founded on atomic strain origins. In this article, we, therefore, focus directly on the strain instead.

Strain is a potential metric to bridge the gap between the atomic scale alterations and the macroscopic response because it is both a microscopic and macroscopic observable.[29] In addition, strain fields can be relatively extensive, given that the volume over which the deformation occurs extends over length scales far beyond the disorder they originate from,[30] ranging from a few ångströms up to the whole crystal.[31] For instance, some of us recently developed the in silico strain engineering protocol to visualize and understand how atomic alterations in a material induce dynamic strain fields that alter the material's polymorphism and macroscopic function.[32] We therein adopted the strain-engineering concept to demonstrate how correlated linker vacancies in the UiO-66 material introduce molecular crumple zones that focus the strain upon pressurization and stabilize the remainder of this material.

Herein, we adopt in silico strain engineering to assess with which magnitude and over what spatial range local atomic substitutions deform and strain the material and can, hence, potentially alter the phase stability of the material. First, we
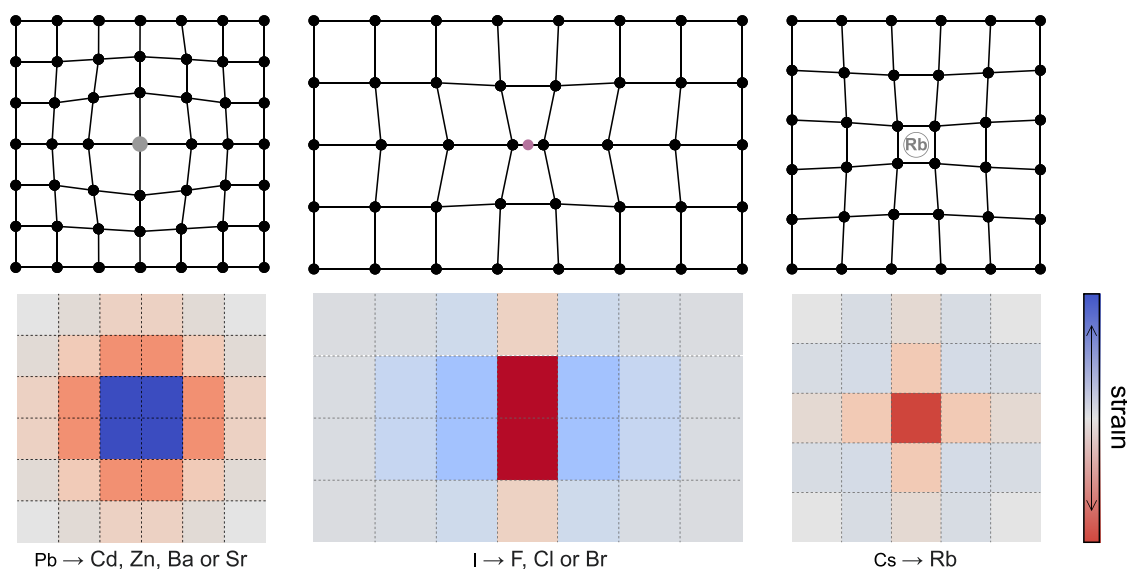
Figure 2. Three illustrative, fictitious strain fields arising from a single lead, iodine, or cesium substitution in a 6 × 6, 7 × 4, and 5 × 5 supercell, respectively. Supercells are chosen to be as small as possible, but they do still capture the most important strain effect. The upper panels show 2D representations of the time-averaged structures with a single-atom substitution. All black dots represent lead atoms used as anchor points for the strain subcells; 2D representations of the strain fields corresponding to these structures are presented underneath. Every cell is colored by its strain, going from high compressive strain (red) via strain-free (gray) to high tensile strain (red). At the bottom, all atom substitutions considered in this work are indicated.

describe the strain fields induced by individual atom substitutions with the same oxidation state as the original atoms. These "elementary" deformations produce a global volume effect that correlates predominantly with the difference in ionic radii of the original and substituted atoms. Despite this qualitative correlation, the strain predicted based on these ionic radii is consistently much larger than the one observed through our simulations, confirming the limits of geometric predictors such as the Goldschmidt tolerance factor. Second, we focus on local information contained in the intrinsic strain fields induced by different atomic substitutions and show that they can be characterized via the Lagrangian strain tensors encompassing the disorder. The magnitude of the strain tensor is observed to decay exponentially when moving away from the substitution, with a decay rate largely independent of the specific atom substitution. Next, we assess in how far the strain arising from a single-atom substitution is altered when additional atom substitutions are present within the crystal. We establish that the strain due to multiple atom substitutions is additive; that is, the strain induced by a double atom substitution can be predicted by summing the strain fields of the individual substitutions. Finally, this strain additivity concept can be generalized: viewing an individual atom substitution as a 0D point defect, multiple atom substitutions can be placed in a variety of 0D, 1D, or 2D geometries to simulate higher dimensional or more complex strain sources. We illustrate via a case study that our strain-engineering approach can accurately predict such complex strain fields from the constituting atomic substitutions. As a result, our strain engineering approach forms an attractive tool to understand and predict how different strain sources may deform and alter the macroscopic $CsPbI_3$ behavior and can hence be adopted to design strain sources that effectively hinder the undesired black-to-yellow phase transition and stabilize the attractive black perovskite phase.

2. METHODS

Two ingredients are essential to predict the strain effects induced by any spatially extended strain source. First, a strain metric must be introduced to quantify the strain from the atomic to the macroscopic level. We will present in Section 2.1 strain fields based on the Lagrangian strain tensor, which satisfies this requirement. Second, our description of the interatomic interactions needs to be sufficiently accurate to describe potential bond breaking upon atomic substitutions in $CsPbI_3$ while simultaneously allowing us to describe spatially extended systems. To fulfill these aims, we will motivate our choice of machine learning potentials (MLPs) in Section 2.2. Figure 2

conceptually visualizes our aim, showing illustrative strain fields that may arise by substituting a single lead (left), iodine (middle), or cesium atom (right). Finally, Section 2.3 reports the computational details used to perform the simulations reported in this work.

2.1. Lagrangian Strain Field Determination. We aim to quantify the effect of any strain source by introducing so-called strain fields. To this end, following the procedure outlined in ref 32, the whole material is first partitioned into so-called voxels or "subcells". For the $CsPbI_3$ material discussed here, we define such a subcell based on the eight PbI_6^{4-} octahedra encompassing any cesium-containing cavity in $CsPbI_3$. This subcell definition corresponds to the definition of the unit cell of the α phase of $CsPbI_3$ but is only a fraction of the unit cell for all other, less symmetric $CsPbI_3$ phases. Specifically, every subcell is characterized by its cell matrix $\mathbf{h} = [\mathbf{a},\mathbf{b},\mathbf{c}]^T$, constructed from the coordinates of the lead atoms in the PbI_6^{4-} octahedra that define that subcell. The lead atoms are chosen as reference points, as they have the smallest thermal vibrations. The subcell matrix is constructed such that each of the three lattice vectors is an average of four cuboid edges, as outlined in more detail in Section S4 of the Supporting Information.

Second, in each of these subcells, and at each time instant t in our dynamic simulations, the Lagrangian strain tensor $\boldsymbol{\eta}(t)$ is calculated. To this end, we first define for each subcell and at each time instant, the deformation gradient $\mathbf{F}(t) = \mathbf{h}(t)\mathbf{h}_0^{-1}$, which describes the deformation of the current subcell matrix $\mathbf{h}(t)$ with respect to a predefined reference subcell matrix $\mathbf{h}_0$. This deformation gradient can then be transformed to the rotation-independent Cauchy deformation tensor $\mathbf{C}(t) = \mathbf{F}^T(t)\mathbf{F}(t)$. When the subcell is unstrained, the Cauchy deformation tensor equals the identity matrix $\mathbf{C}(t) = \mathbf{I}$. To quantify to which extent $\mathbf{C}$ differs from $\mathbf{I}$, the Lagrange finite strain tensor is evaluated as $\boldsymbol{\eta}(t) = \frac{1}{2}(\mathbf{C}(t) - \mathbf{I})$.

At this point, it is illustrative to derive the strain tensor explicitly for a simple case study. To this end, consider an orthorhombic reference subcell $\mathbf{h}_0$, with lattice vectors $\mathbf{a} = [a_x,0,0]^T$, $\mathbf{b} = [0,b_y,0]^T$, and $\mathbf{c} = [0,0,c_z]^T$, and a deformed subcell $\mathbf{h}$ with lattice vectors $\mathbf{a} + \mathrm{d}\mathbf{a}$, $\mathbf{b} + \mathrm{d}\mathbf{b}$, and $\mathbf{c} + \mathrm{d}\mathbf{c}$. In this case

$$\mathbf{h}_0 = \begin{bmatrix} a_x & 0 & 0 \\ 0 & b_y & 0 \\ 0 & 0 & c_z \end{bmatrix} \text{ and } \mathbf{h} = \begin{bmatrix} a_x+\mathrm{d}a_x & \mathrm{d}a_y & \mathrm{d}a_z \\ \mathrm{d}b_x & b_y+\mathrm{d}b_y & \mathrm{d}b_z \\ \mathrm{d}c_x & \mathrm{d}c_y & c_z+\mathrm{d}c_z \end{bmatrix} \quad (1)$$

This leads to the following Lagrangian strain tensor

$$\boldsymbol{\eta} = \begin{bmatrix} \dfrac{\mathrm{d}a_x}{a_x} + \dfrac{\mathrm{d}a_x^2+\mathrm{d}b_x^2+\mathrm{d}c_x^2}{2a_x^2} & \dfrac{\mathrm{d}a_y}{2b_y} + \dfrac{\mathrm{d}b_x}{2a_x} + \dfrac{\mathrm{d}a_x\mathrm{d}a_y+\mathrm{d}b_x\mathrm{d}b_y+\mathrm{d}c_x\mathrm{d}c_y}{2a_xb_y} & \dfrac{\mathrm{d}a_z}{2c_z} + \dfrac{\mathrm{d}c_x}{2a_x} + \dfrac{\mathrm{d}a_x\mathrm{d}a_z+\mathrm{d}b_x\mathrm{d}b_z+\mathrm{d}c_x\mathrm{d}c_z}{2a_xc_x} \\[3ex] \dfrac{\mathrm{d}a_y}{2b_y} + \dfrac{\mathrm{d}b_x}{2a_x} + \dfrac{\mathrm{d}a_x\mathrm{d}a_y+\mathrm{d}b_x\mathrm{d}b_y+\mathrm{d}c_x\mathrm{d}c_y}{2a_xb_y} & \dfrac{\mathrm{d}b_y}{b_y} + \dfrac{\mathrm{d}a_y^2+\mathrm{d}b_y^2+\mathrm{d}c_y^2}{2b_y^2} & \dfrac{\mathrm{d}b_z}{2c_z} + \dfrac{\mathrm{d}c_y}{2b_y} + \dfrac{\mathrm{d}a_y\mathrm{d}a_z+\mathrm{d}b_y\mathrm{d}b_z+\mathrm{d}c_y\mathrm{d}c_z}{2b_yc_z} \\[3ex] \dfrac{\mathrm{d}a_z}{2c_z} + \dfrac{\mathrm{d}c_x}{2a_x} + \dfrac{\mathrm{d}a_x\mathrm{d}a_z+\mathrm{d}b_x\mathrm{d}b_z+\mathrm{d}c_x\mathrm{d}c_z}{2a_xc_z} & \dfrac{\mathrm{d}b_z}{2c_z} + \dfrac{\mathrm{d}c_y}{2b_y} + \dfrac{\mathrm{d}a_y\mathrm{d}a_z+\mathrm{d}b_y\mathrm{d}b_z+\mathrm{d}c_y\mathrm{d}c_z}{2b_yc_z} & \dfrac{\mathrm{d}c_z}{c_z} + \dfrac{\mathrm{d}a_z^2+\mathrm{d}b_z^2+\mathrm{d}c_z^2}{2c_z^2} \end{bmatrix}$$

$$(2)$$

All elements of the strain tensor have both linear and quadratic displacement terms and are thus, in general, not additive.

However, suppose we can assume that the individual atomic displacements are sufficiently small,[30] so that the quadratic terms

can be neglected with respect to the linear terms. In that case, the strain tensor reduces to

$$\eta' = \begin{bmatrix} \dfrac{da_x}{a_x} & \dfrac{da_y}{2b_y} + \dfrac{db_x}{2a_x} & \dfrac{da_z}{2c_z} + \dfrac{dc_x}{2a_x} \\[2ex] \dfrac{da_y}{2b_y} + \dfrac{db_x}{2a_x} & \dfrac{db_y}{b_y} & \dfrac{db_z}{2c_z} + \dfrac{dc_y}{2b_y} \\[2ex] \dfrac{da_z}{2c_z} + \dfrac{dc_x}{2a_x} & \dfrac{db_z}{2c_z} + \dfrac{dc_y}{2b_y} & \dfrac{dc_z}{c_z} \end{bmatrix} \tag{3}$$

From eq 3, it is clear that if the strain tensor is perfectly linear with respect to the deformation induced by the strain source, the global strain field induced by combining different strain sources can be obtained by simply adding the individual strain fields. However, in practice, eq 3 is valid only in the limit of infinitesimal strains. Since any practical strain source induces finite strains, we expect deviations from this perfect additivity. Hence, the fundamental question from a practical point of view is to which extent the approximation of strain additivity still holds when finite strain sources are present in the system. It is exactly this question we wish to answer in this work, by focusing on individual strain fields induced by atomic substitutions.

2.2. Machine Learning Potentials. A careful determination of a strain field is a computationally challenging problem, as the strain extends over several unit cells. Furthermore, perovskite structures are characterized by shallow free energy minima[33,34] and the strain in these materials fluctuates appreciably due to thermal vibrations (see Section S2 of the Supporting Information). As a result, describing these dynamic strain fields requires dynamic simulations rather than static relaxations, which would optimize to a local minimum. Moreover, these dynamic simulations should be sufficiently long to obtain statistically meaningful results. These required simulation times are prohibitive for ab initio molecular dynamics (MD) simulations of such extended structures, even at the density functional theory (DFT) level. However, it would also be challenging to use force field methods. Due to the large variety of chemical elements, many different force field parameters would have to be optimized. Furthermore, large local deformations and even potential bond reorganization occur in the proximity of the atom substitutions that are difficult or even impossible to capture with force fields,[35] especially when the atomic radius of the substituent is significantly different from the original atom. For these reasons, MLPs that learn the structure−energy relation by training a neural network on ab initio data are an ideal approach.[33,36,37] In the first place, MLPs exhibit high accuracy even when large structural deformations occur, conditional on these deformations forming part of the training set. Second, MLPs are fast enough to allow for sufficiently long MD simulations. The applicability of MLPs to the CsPbI$_3$ system has also been shown before.[33,38]

In this work, we used Neural Equivariant Interatomic Potentials (NequIP)[39,40] MLPs that are based on E(3)-equivariant graph neural networks. These MLPs are very data efficient such that highly accurate MLPs can be trained with relatively small data sets. MLPs are trained on short ab initio MD trajectories, and subsequently, strain fields are evaluated on longer MD simulations by using the trained MLPs. While we could, in principle, train one MLP for all possible atomic substitutions considered in this work (Figure 2), this would lead

to a combinatorial explosion of possible interatomic interactions. This combinatorial explosion can be circumvented, as we restrict ourselves to one or two types of substituted atomic species for any given strain-engineered perovskite. Specifically, as outlined in Section S1 of the Supporting Information, we trained separate MLPs for each set of one or two atomic species of substituents.

2.3. Computational Details. Our computational procedure consists of four steps. First, a diverse training and validation set for each of the MLPs is derived by performing ab initio MD simulations on small CsPbI$_3$ cells containing one or two atomic substitutions. Second, this data set is used to train and validate the MLP. Third, the MLPs are used to perform MD simulations on larger systems. Fourth, the strain fields are determined from MLP-MD simulations.

2.3.1. MLP Training Set Generation. Our reference system used to generate the data sets is the γ phase of CsPbI$_3$, as it is the most stable black phase at room temperature.[7,41] The unit cell is rotated such that the axes are almost parallel to the Pb−I−Pb bonds (except for the tilting), and a supercell is constructed such that a 320-atoms cell of $4 \times 4 \times 4$ CsPbI$_3$ subcells, as defined in Section 2.1, is formed. Formally, the $4 \times 4 \times 4$ supercell corresponds to a conventional γ-CsPbI$_3$ unit cell transformed via the matrix: $\begin{pmatrix} 2 & -2 & 0 \\ 2 & 2 & 0 \\ 0 & 0 & 2 \end{pmatrix}$. In the remainder of this article, supercell sizes are provided analogously. To generate each MLP data set, ab initio *NVT* calculations, each with a simulation time of 2−6 ps, are performed at an elevated temperature of 800 K and at a range of volumes, varying from 90 to 120% of the reference volume. In each MD simulation, one or two atoms are substituted. When two atoms are substituted, we consider various relative orientations. Snapshots from each ab initio MD simulation are combined into a single training data set, which consists of the energies and forces of these snapshots. Another validation set of five MD simulations is performed with reference volumes within the range present in the training data but with different substitution positions to obtain an uncorrelated validation set for the MLP training.

All DFT calculations are performed using the CP2K software[42] via the combined Gaussian and plane wave (GPW)[43] method with TZVP-MOLOPT-SR-GTH basis sets[44] and GTH pseudopotentials.[45] The CP2K MULTIGRID method is used with five grids of increasing fineness, with the finest grid having an energy cutoff of 400 Ry and the reference level for mapping the Gaussians to the multigrid being set to 40 Ry. The Perdew−Burke−Ernzerhof exchange−correlation functional[46] is used together with Grimme et al.'s D3 dispersion correction and Becke−Johnson damping,[46−48] as this PBE-D3(BJ) combination is shown to give accurate results for CsPbI$_3$ with respect to a random phase approximation + Hartree−Fock (RPA + HF) reference, as shown in ref 33. All CP2K MD simulations were performed within the *NVT* ensemble using a time step of 1 fs and a Nosé−Hoover thermostat with a time constant of 100 fs and a chain of three thermostat beads. The volume constraint in this ensemble mimics more closely the restoring forces exerted by the material regions away from the strain source in the simulation cell. The temperature was set to *T* = 800 K, which is significantly higher than the 300 K production simulations, to get a diverse sampling of the configurational phase space. This cell is sufficiently large that a single *k*-point (at the Γ-point) can be used.

2.3.2. MLP Training. After the training and validation sets are obtained from snapshots of the DFT-based MD simulations, the

MLPs are trained with the NequIP deep-learning approach.[39,40] The MLPs are trained on the energies and the forces of the data set. Training on the stresses only deteriorated our results and was therefore not included. All MLPs are generated with a radius cutoff of 7 Å, 3 interaction blocks, 16 features, a learning rate of 0.005, a batch size of 5, and a maximum irreducible representation order for the network's features l_{max} being 1. The loss coefficient ratio between the energy and forces is set to 1. After training each MLP, a short 10 ps MD simulation is performed with the MLP from which snapshots are re-evaluated with CP2K to assess the error on new configurations not visited during the training. The results of these final tests are reported in Section S1 of the Supporting Information.

2.3.3. MLP MDs. The MLP-MD simulations are performed by coupling NequIP to our in-house MD engine YAFF[49] via the atomic simulation environment (ASE).[50] Unless otherwise specified, these MD simulations are performed within the *NPT* ensemble at a pressure of $P = 1$ bar and a temperature $T = 300$ K. The time step used during the MLP-MD runs was 1 fs. A Langevin thermostat with a time constant of 100 fs and a Langevin barostat with a time constant of 1 ps ensured temperature and pressure control during these simulations. Our choice to perform these simulations in the *NPT* rather than in the *NVT* ensemble is based on the volume constraints in the latter. In the *NVT* ensemble, each decrease in volume at any given point in the material is artificially compensated elsewhere to ensure that the total simulation volume remains constant.

2.3.4. Strain Field Generation and Visualization. To evaluate the strain induced by single atomic substitutions, we first performed *NPT* MLP-MD simulations on a supercell containing $4 \times 4 \times 4$ perovskite cuboids. For each type of atom substitution, the volume deviation is obtained from time-averaging the cell parameters of ten 100 ps MLP-MD simulations at 300 K with different random initial velocities. In these simulations, also the instantaneous strain tensor is evaluated for each subcell and at each time instant and subsequently averaged to obtain the time-averaged 3D strain fields reported here. Although the difference in tilting angles and lattice vectors along the different dimensions in $CsPbI_3$ is important in determining the electronic properties of the material,[7] the strain fields are highly symmetrical as shown in Section S5 of the Supporting Information. For the systems with two atomic substitutions, a $4 \times 4 \times 12$ supercell was used. In this case, the presented strain fields are averaged over the $12 \times 4 \times 4$, $4 \times 12 \times 4$, and $4 \times 4 \times 12$ supercells, rotated such that the z-direction is along the long cell axis of 12 cells. Note that these systems are only identical when the perovskite is in the α phase as the *a*, *b*, and *c* axes are not the same in the β and γ phases. Along each direction, ten 100 ps MD simulations are performed with different random initial velocities. Thus, the $4 \times 4 \times 12$ strain fields are averaged over 3×10 MD simulations, yielding a total time of 3 ns. As the $4 \times 4 \times 4$ strain fields for the single-atom substitutions show periodic boundary effects, also the strain introduced by these monatomic substitutions was evaluated in the aforementioned $4 \times 4 \times 12$ supercells.

3. RESULTS AND DISCUSSION

3.1. Global Strain Effects Induced by Single-Atom Substitutions and Limitations of the Goldschmidt Tolerance Factor. Before investigating the local strain fields at the individual subcell level, we will first focus on the macroscopic volumetric strain of the whole γ-$CsPbI_3$ system induced by different single-atom substitutions. Besides directly

predicting the volumetric strain from our MLP-MD simulations, we also predict the expected volume deviations due to single-atom substitutions based solely on the atomic radii of the ions present in the material. To this end, we assume that the perovskite lattice vectors scale according to the sum of the ionic radii, in analogy with the Goldschmidt tolerance factor. Specifically, for a B-site (Pb^{2+}) or X-site (I^-) substitution, the rescaled lattice vector is correlated to $l_{BX} = r_B + r_X$, with r_B and r_X being the atomic radii of the atoms on the B and X sites, respectively. For an A-site (Cs^+) substitution, the rescaled lattice vector is given by $l_{AX} = (r_A + r_X)/\sqrt{2}$, with r_A being the atomic radius of the A-site cation, instead. Based on our assumption and the observation that the atomic radii are simply summed in the two formulas for the lattice vector defined above, the lattice vector obtained when substituting a new ion Q′ for an existing ion Q in $CsPbI_3$ can be theoretically predicted as

$$l_{PQ'} = \frac{r_P + (1-f)r_Q + fr_{Q'}}{r_P + r_Q} l_{PQ} \tag{4}$$

In this expression, $l_{PQ'}$ and l_{PQ} are the scaled and reference lattice vectors of the material calculated via one of the formulas mentioned above (depending on the site where the ion substitution takes place), and *f* is the effective doping fraction. For our single substitutions in the $4 \times 4 \times 4$ materials, *f* equals 1/64. The predicted volume change of a single-atom substitution can now be derived straightforwardly from the rescaled lattice vector calculated in eq 4. For lead and cesium substitutions, which affect the three directions equally, $\Delta V_{pred} = l_{PQ'}^3 - l_{PQ}^3$. In contrast, for the iodine substitutions, we assume that only the lattice vector aligned with the substituted Pb–I–Pb motif changes, such that $\Delta V_{pred} = l_{PQ'}l_{PQ}^2 - l_{PQ}^3$.

Figure 3 illustrates that the volume changes predicted this way are around 3−4 times larger than those obtained directly from
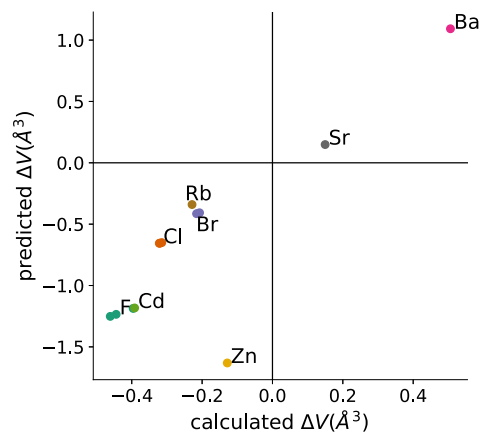

Figure 3. Comparison of the absolute volume differences per unit cell as predicted theoretically via eq 4 and as obtained from our MLP-MD simulations. For the halogen substitutions, three (very similar) values are reported, corresponding to the substitution of the three symmetrically different iodine positions.

the MLP-MD simulations, while the latter are on the same order of magnitude and sign as measured experimentally (see Section S3 of the Supporting Information). The mismatch between our predicted volume changes and those extracted from the MLP-MD simulations is expected, as our prediction does not consider any structural relaxation occurring during the MD simulation. Nevertheless, the obtained volume differences clearly follow the
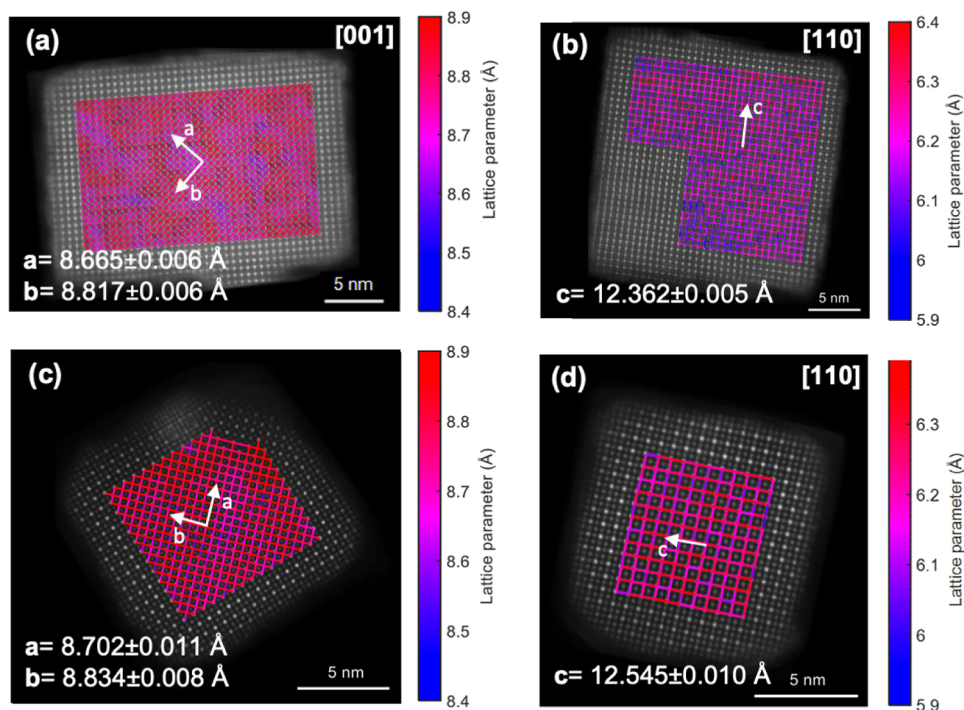
Figure 4. High-resolution HAADF STEM images for (a,b) pure $CsPbI_3$ and (c,d) for 10% Zn-doped $CsPbI_3$ with corresponding lattice parameters analysis overlays. For both the doped and undoped materials, both the [001] (a,c) and [110] (b,d) zone axes are reported. Along both zone axes, an increase in lattice parameters is observed for the zinc-doped material despite the smaller ionic radius of zinc compared with lead. The details of experimental work with these two materials are presented in Section S9 of the Supporting Information.
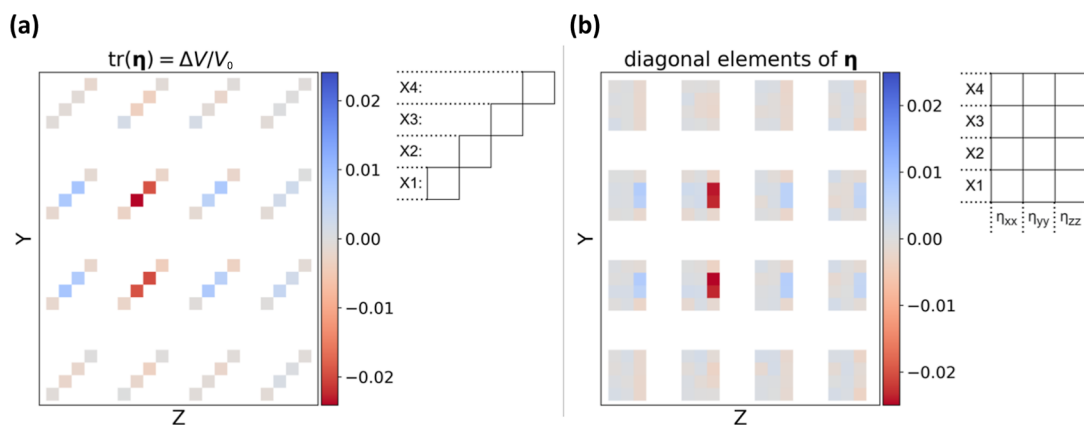

Figure 5. Color maps of the 3D strain field resulting from a single $I \rightarrow Cl$ substitution in a $4 \times 4 \times 4$ supercell. (a) Trace of the Lagrangian strain tensor for each of the $4 \times 4 \times 4$ subcells, where different subcells along the x direction are presented along the diagonals. (b) Diagonal elements of Lagrangian strain $\boldsymbol{\eta}$. For each 3×4 block belonging to subcells at a given (y, z) coordinate pair, moving vertically in the block equals consecutive cells in the x-direction, while moving horizontally, one encounters, from left to right, η_{xx}, η_{yy}, and η_{zz}, respectively.

trend that the larger the difference in atomic radii between the original and substituted atoms, the larger the volume difference. However, zinc is a remarkable exception. Zinc (74 pm) has a much smaller atomic radius than lead (119 pm), which leads to a significant predicted volume difference. However, our MD simulations indicate that the volume difference upon zinc substitution is much smaller. This hints toward the breakdown of our assumption that the volume deviation correlates with effective radii, as expressed in eq 4. We hypothesize two effects that may cause this breakdown. First, when lead ions are substituted for zinc ions, some Zn−I bonds break, thus causing a local structural deformation instead of straining the whole structure. Second, given the exceptionally small size of the zinc ions, they may also migrate to interstitial positions on longer

time scales, thereby preserving the original $CsPbI_3$ framework with only a small volume change. While the exact location of zinc dopants in $CsPbI_3$ remains an open question in the literature, the hypothesis that zinc may occupy interstitial positions is indirectly confirmed by our high-angle annular dark field scanning transmission electron microscopy (HAADF-STEM) images, shown in Figure 4. Upon doping $CsPbI_3$ with 10% zinc, the lattice parameters increase by 0.40, 0.19, and 1.48%, respectively, resulting in a 2.1% volume increase. As zinc is smaller than the lead ions it replaces, this hints toward zinc occupying the interstitial positions rather than purely replacing the lead ions.

The quantitative mismatch between the predicted and simulated volume differences in Figure 3 reveals the deficiencies of using the Goldschmidt factor (or similar static metrics used to
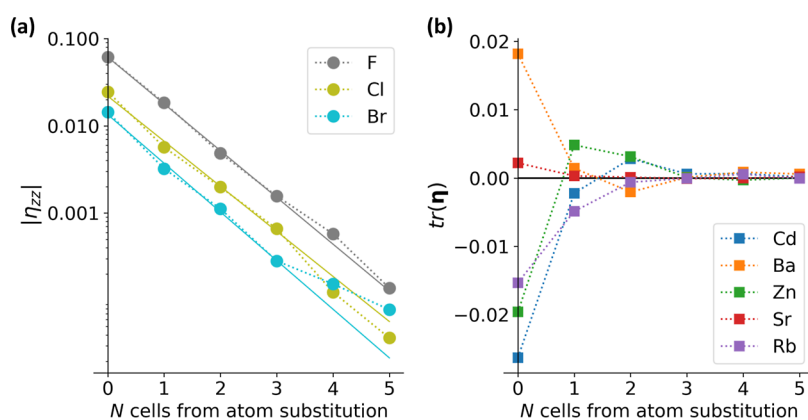
Figure 6. Evolution of the Lagrangian strain as a function of the distance of the subcell from the substitution. (a) $|\eta_{zz}|$ component for fluorine, chlorine, and bromine substitutions along the z-direction. An exponential fit is provided for each substitution based only on the first four data points ($N \leq 3$). The absolute value of η_{zz} is given such that the strongly negative strain of the zeroth subcell (containing the I → X substitution) changes sign. For all other points, $\eta_{zz} = |\eta_{zz}|$. (b) tr($\boldsymbol{\eta}$) volumetric strains for the metal dopants.
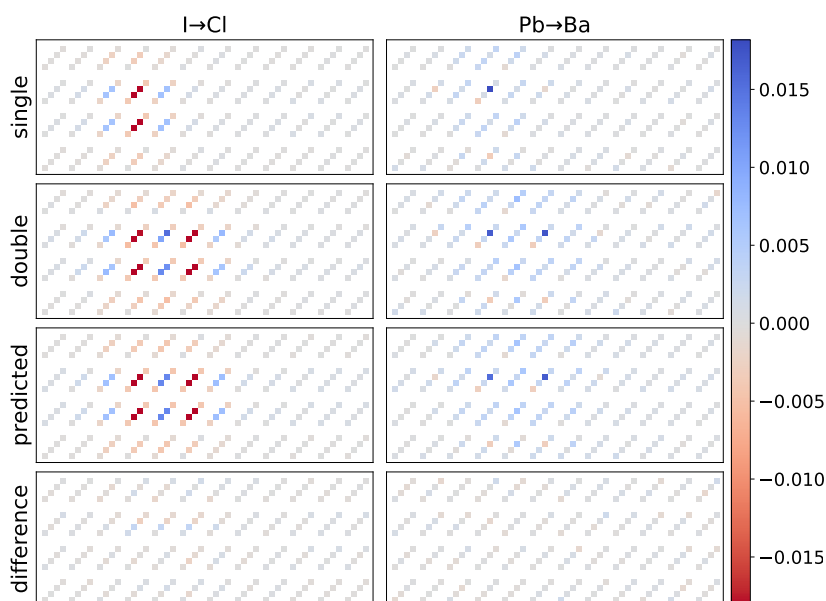

Figure 7. Strain fields corresponding to I → Cl and Pb → Ba substitutions in a $4 \times 4 \times 12$ CsPbI$_3$ supercell, represented with the trace of the Lagrangian strain tensor. Axis units and dimensions are the same as detailed in Figure 5 except that the z-direction is now 12 instead of 4 unit cells long. The first row shows the MLP-MD results with a single dopant. The second row shows the MLP-MD result with two dopants, with the second dopant placed two unit cells further along the z-axis. The third row shows the sum of the first-row strain field with the same first-row strain field but now translated to the second dopant position. The fourth row shows the remainder of the subtraction of the second row from the third row. Note that for the Pb → Ba plots, the subcell is translated over half a unit cell such that the A sites are at the center of the cell. As a result, only one subcell per lead substitution is heavily strained (see also the comparison of subcell definitions in Section S4 of the Supporting Information).

predict the effect of atomic substitutions in perovskites) in predicting the strain and hence relative stability of substituted perovskites. As a result, it demonstrates the need for a more accurate technique, such as the strain-engineering approach discussed here.

3.2. Spatial Extent of Strain Fields Induced by a Single-Atom Substitution. To illustrate the information obtained with local Lagrangian strain fields, we first focus on a single I → Cl X-site substitution along a Pb−I−Pb motif that aligns with the z-direction in a $4 \times 4 \times 4$ supercell. Figure 5 visualizes the strain field obtained from the MLP-MD simulations. Specifically, Figure 5a shows the relative volume deviations, which correspond to the trace of the Lagrangian strain tensor. In contrast, Figure 5b reports the three diagonal elements η_{xx}, η_{yy}, and η_{zz} of strain $\boldsymbol{\eta}$, which indicate uniaxial strains. Because the

new Pb−Cl bond is significantly shorter than the original Pb−I bond and because the substituted Pb−Cl−Pb motif borders four different subcells, four subcells in Figure 5a experience a decrease in volume amounting to 1−2%. Along the direction of the substituted Pb−Cl−Pb motive (in casu, the z-direction), subcells that neighbor these four subcells experience a slight increase in volume (<1%) instead. Figure 5b further illustrates that these volume increases and decreases can be solely attributed to changes in the η_{zz} component for each subcell. This reveals that the halide substitutions mainly affect the strain along the direction defined by the two lead atoms that neighbor the substituted ion (in casu, the z-direction). The magnitude of this strain strongly depends on the considered CsPbI$_3$ phase, as shown for instance for a single I → Cl substitution in δ-CsPbI$_3$ in Section S7 of the Supporting Information.
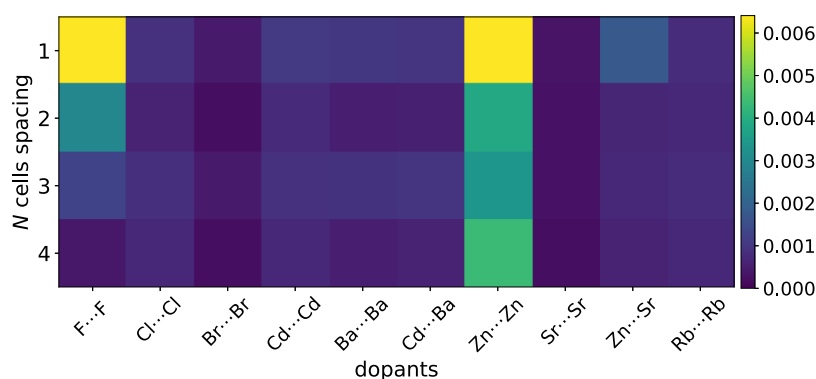
Figure 8. RMSEs between the simulated strain fields induced by a double-atom substitution and the strain field predicted by adding two single-atom substitutions as a function of the dopants and the spacing between the two dopants.

While Figure 5 demonstrates the potential of strain fields to provide local information on the strain introduced by single-atom substitutions, it also reveals that $4 \times 4 \times 4$ supercells are too small to assess the long-range strain effects of the atom substitutions. In both panels, it is clear that the periodic boundary conditions, especially in the z-direction, overlap the strain experienced by the different periodic images. As this is also true for A- and B-site substitutions, albeit to a lesser extent, we will evaluate in what follows the strain effect of all types of atom substitutions in larger $4 \times 4 \times 12$ cells.

Figure 6 depicts how the magnitude of the strain changes along the z-direction (containing 12 subcells) as a function of the number of subcells N moving away from the atom substitution. At the location of the substituted atom, all substitutions cause a local compressive strain, except for barium and strontium, for which the strain is positive for $N = 0$. For halogen substitutions, the strains are about 1 order of magnitude larger than for metal substitutions. In all cases, the strain rapidly decreases with respect to the distance from the atom substitution. For the halogens, this decay is almost perfectly exponential, with exponential decay rates of 1.17, 1.16, and 1.16 per subcell for F, Cl, and Br, respectively. For the metal substitutions, the absolute strain values are an order of magnitude smaller and the strains further away from the dopant ($N \geq 2$) are too small to accurately determine the strain decay rate. However, they appear to decay faster. Interestingly, the strain decay rates corresponding to the halogen substitutions are all very similar. Thus, the decay rates appear not to depend on the substituted ion but are rather a material constant, characteristic of the specific substitution position and the nature of the material.

3.3. Additivity in Strain Fields from Double Atom Substitutions. Given that strain fields can capture the effect of single-atom substitutions, the question arises of how strain fields induced by different sources interact. Specifically, can the total strain field generated by a double-atom substitution be predicted by summing the strain fields of each individual single-atom substitution? To answer this question, we performed simulations for both single- and double-atom substitutions. For the double-atom substitutions, the second atom substitution is placed at a distance of one, two, three, or four subcells from the first atom substitution along the longest dimension of the supercell. The two substituted atoms are always the same ions, except for the (Cd,Ba) and (Zn,Sr) pairs that we also consider.

As an illustrative example, Figure 7 visualizes the strain fields induced by either I → Cl or Pb → Ba substitutions. For both substitutions, the top row shows the strain field with a single-atom substitution, while the second row shows the strain fields

with two substitutions being placed two cells away from each other. In the third row, the predicted strain field induced by two ion substitutions is visualized. This prediction is obtained by adding two monosubstituted strain fields of the first row together, with the second one being translated to the location of the second atom substitution. The bottom row of Figure 7 shows the difference between the actual strain field of the second row and the predicted strain field of the third row for double atom substitutions. In the case of perfect additivity, the strain fields of the fourth row should be zero.

At first sight, the bottom row in Figure 7 reveals only small deviations between the predicted and the actual strain fields. This indicates that the quadratic terms arising in the Lagrangian strain tensors are indeed negligible and that strain fields induced by monatomic substitutions are strongly additive. For all other substitutions, the strain fields with the second dopant placed at different distances as well as plots of all the diagonal and shear components of the strain tensors are visualized in Section S6 of the Supporting Information.

To quantify these observations, Figure 8 visualizes the root-mean-square errors (RMSEs) between the strain field obtained directly by a double-atom substitution on one hand and the strain field predicted by summing the strain fields of two single-atom substitutions on the other hand. Next to the substitutions presented in Figure 7, we vary in Figure 8 also the distance between the two substitutions, from one to four subcells, as well as the substituted species. All raw strain fields used to generate Figure 8 are reported in Section S6 of the Supporting Information.

Overall, Figure 8 underscores our hypothesis that the strain fields induced by single-atom substitutions are largely additive. However, two substitutions show larger errors. The largest RMSE is observed for two neighboring I → F substitutions. This is due to the bond breaking occurring for this substitution because the Pb−F bond is much shorter than the Pb−I bond and thus snaps due to the large strain. When the I → F substitutions are further apart, the additivity improves. The Pb → Zn substitutions cause large structural deformations, resulting in time-averaged structures where the zinc atoms move far away from the original lead position and whereby at least one Zn−I bond is broken. As shown in Section S8 of the Supporting Information, some of these zinc dopants even tend to move toward the interstitial positions, as hypothesized above. This causes a highly anisotropic strain field and, since one does not know a priori which of the six equivalent Zn−I bonds will break, poor additivity. In the absence of random symmetry breaking as introduced by the I → F and Pb → Zn substitutions, however,
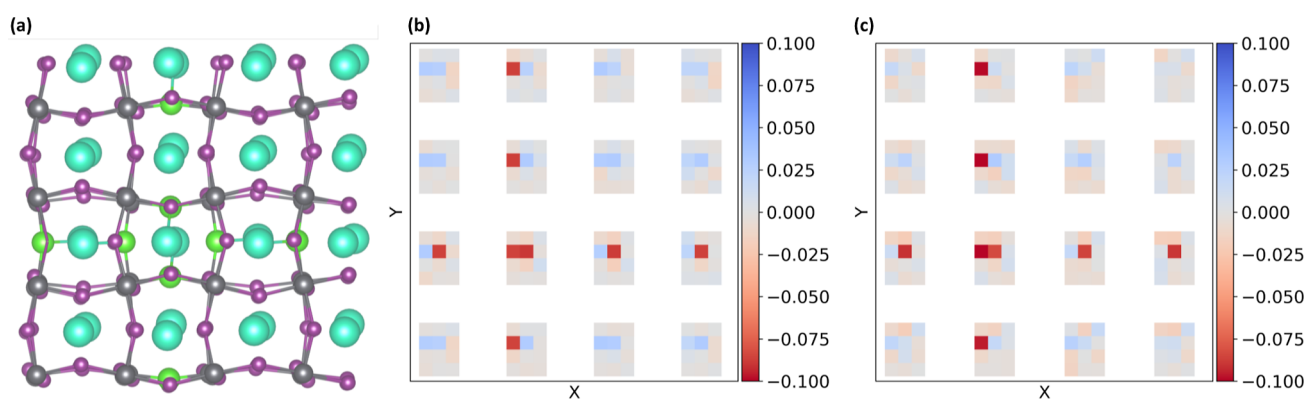
Figure 9. Case study of the strain field additivity for more complex strain fields. (a) Atomic structure of the considered material with eight I → Cl substitutions viewed along the z axis. (b,c) Diagonal η_{xx}, η_{yy}, and η_{zz} components of Lagrangian strain fields (b) obtained directly from the fully substituted MLP-MD simulations or (c) predicted by summing the eight individual strain fields induced by single I → Cl substitutions.

our results indicate that the investigated strain fields are largely additive.

3.4. Case Study on the Strain Field Additivity for More Complex Strain Fields. Now that we have established that the strain fields are additive using solely two atom substitutions, more sophisticated atomic arrangements can be assessed. As iodine substitutions predominantly cause strain in one direction, while lead and cesium substitutions strain all directions evenly, the iodine substitutions allow for greater tunability. This directionality of the iodine position allows us to create specific 1D or 2D strain fields. Although this specific iodine substitution pattern and the resulting strain field may be challenging to reproduce experimentally, they may offer valuable insights into how strain can affect phase stability if full control over the atomic structure of these materials could be reached. Also, some arrangements of substitutions can be used to approximate more complex experimental strain fields. For example, introducing a layer of iodine substitutions might produce mechanically similar strains to those obtained from adhering the perovskites to a strained interface. This allows us to probe a diversity of strain fields without the additional intricacies of interface effects and training MLPs for specific interfaces.

As an example of a more sophisticated strain field, a $4 \times 4 \times 12$ structure is constructed with eight I → Cl substitutions, all placed within the same (third) (x, y)-plane, as visualized in Figure 9a. Due to the local character of the strain, only the strain in the first four (x, y) layers substantially deviates from zero and is presented. The strain fields as simulated directly via MLP-MD simulations, shown in Figure 9b, and as predicted from the sum of eight strain fields from a single substitution, shown in Figure 9c, are indeed very similar. This further confirms the potential of strain additivity to predict strain fields induced by complex strain sources.

4. CONCLUSIONS

Various experimental strain-based techniques have recently emerged to stabilize the black $CsPbI_3$ phase. Yet, the need for more information on how these successful techniques introduce strain throughout the material from the atomic to the macroscopic level impedes optimizing phase control in these materials further. To overcome this hurdle, in this work, we combined an in silico strain-engineering approach with newly derived MLPs to assess the strain induced by atomic substitutions in $CsPbI_3$ as "elementary" strain sources. We started by demonstrating that the global strain induced by these

atomic substitutions correlates well with the difference in ionic radii, except in the case of Pb → Zn substitutions, due to the excessive difference in ionic radii, which causes the breaking of the Zn−I bonds. Although a correlation was found, the effective strain was, in all cases, much smaller than the one predicted solely based on ionic radii. This demonstrates that metrics relying on these radii, such as the Goldschmidt tolerance factor, have only limited applicability when aiming to predict dynamic strain fields and that more quantitative prediction tools are needed.

From our MLP-MD simulations, we first investigated the magnitude and spatial extent of the strain fields introduced by single-atom substitutions. We found that these strain fields decay exponentially with the distance from the strain source with a decay constant independent of the substituted ion. Next, we demonstrated that the strain fields of these elementary strain sources are additive, as the strain fields induced by double-atom substitutions are similar to the sum of two single-atom substitution strain fields. The only significant deviation from this strain additivity was observed when the strains induced by the atom substitutions were so large that bond breaking occurred. This was, for instance, the case for the Pb → Zn substitutions, as zinc ions moved toward interstitial positions, and for I → F substitutions. Finally, we showed that this strain additivity can be exploited more widely, as demonstrated through a case study, where two rows of iodines were substituted for chlorine.

The additivity of strain fields demonstrated in this work combined with our in silico strain engineering approach provides a valuable tool to model complex strain environments as a sum of strain fields induced by "elementary" strain sources. Our approach paves the way to assess, from the atomic level onward, how complex arrangements of strain sources lead to dynamically evolving strain fields that interact with one another and cooperatively affect the phase stability of the material under study. One of the key strengths of the strain engineering approach presented here is that these strain fields can be designed through various strain sources, such as those induced by atomic substitutions, interfacial mismatch, or surface functionalizations. Hence, while all strain fields aim to impact the atomic vibrations around the strain source and will always affect both the vibrational entropy and enthalpy,[10,33] the extent to which either energy or entropy dominates the strain engineering mechanism entirely depends on the specific strain source being introduced.[51]

Finally, answering the ultimate question of whether the strain additivity observed here also holds in the large-strain regime for which strain fundamentally impacts the phase transition requires one to (i) quantify the impact of the resulting strain fields on the black-to-yellow free energy landscape, (ii) achieve dopant concentrations that are sufficiently high to fundamentally alter the phase energetics, and (iii) realize such computationally informed strain fields experimentally. While these remain open challenges at the moment, we anticipate that our approach may help to rationalize current phase stabilization approaches and to develop new ones for MHPs and other polymorphic materials.

■ ASSOCIATED CONTENT

Data Availability Statement

Computational data supporting the results of this work are available from the Zenodo archive 7696485.[52]

Ⓢ︎ Supporting Information

The Supporting Information is available free of charge at https://pubs.acs.org/doi/10.1021/acs.jpcc.3c05770.

> Validation of the MLPs, comparison with thermal strain fluctuations, comparison of volumetric changes with experimental doping studies, definition of the strain subcell, additional strain field analyses, mobility of the zinc substitution, experimental details of the perovskite nanocrystal synthesis and TEM imaging (PDF)

■ AUTHOR INFORMATION

Corresponding Authors

Johannes L. Teunissen − *Center for Molecular Modeling (CMM), Ghent University, B-9052 Zwijnaarde, Belgium;* ⓞ orcid.org/0000-0002-0188-6064; Email: jlteunissen@gmail.com

Veronique Van Speybroeck − *Center for Molecular Modeling (CMM), Ghent University, B-9052 Zwijnaarde, Belgium;* ⓞ orcid.org/0000-0003-2206-178X; Email: Veronique.VanSpeybroeck@UGent.be

Authors

Tom Braeckevelt − *Center for Molecular Modeling (CMM), Ghent University, B-9052 Zwijnaarde, Belgium; Department of Chemistry, KU Leuven, B-3001 Heverlee, Belgium*

Irina Skvortsova − *Electron Microscopy for Materials Science (EMAT) and NANOlab Center of Excellence, University of Antwerp, B-2020 Antwerp, Belgium*

Jinhui Guo − *Electron Microscopy for Materials Science (EMAT) and NANOlab Center of Excellence, University of Antwerp, B-2020 Antwerp, Belgium*

Bapi Pradhan − *Department of Chemistry, KU Leuven, B-3001 Heverlee, Belgium;* ⓞ orcid.org/0000-0002-6202-7343

Elke Debroye − *Department of Chemistry, KU Leuven, B-3001 Heverlee, Belgium;* ⓞ orcid.org/0000-0003-1087-4759

Maarten B. J. Roeffaers − *Centre for Membrane Separations, Adsorption, Catalysis, and Spectroscopy for Sustainable Solutions, Department of Microbial and Molecular Systems, KU Leuven, B-3001 Heverlee, Belgium;* ⓞ orcid.org/0000-0001-6582-6514

Johan Hofkens − *Department of Chemistry, KU Leuven, B-3001 Heverlee, Belgium; Max Planck Institute for Polymer Research, D-55128 Mainz, Germany;* ⓞ orcid.org/0000-0002-9101-0567

Sandra Van Aert − *Electron Microscopy for Materials Science (EMAT) and NANOlab Center of Excellence, University of Antwerp, B-2020 Antwerp, Belgium*

Sara Bals − *Electron Microscopy for Materials Science (EMAT) and NANOlab Center of Excellence, University of Antwerp, B-2020 Antwerp, Belgium;* ⓞ orcid.org/0000-0002-4249-8017

Sven M. J. Rogge − *Center for Molecular Modeling (CMM), Ghent University, B-9052 Zwijnaarde, Belgium;* ⓞ orcid.org/0000-0003-4493-5708

Complete contact information is available at:
https://pubs.acs.org/10.1021/acs.jpcc.3c05770

Notes

The authors declare no competing financial interest.

■ REFERENCES

(1) Kim, J. Y.; Lee, J.-W.; Jung, H. S.; Shin, H.; Park, N.-G. High-Efficiency Perovskite Solar Cells. *Chem. Rev.* **2020**, *120*, 7867−7918.

(2) Eames, C.; Frost, J. M.; Barnes, P. R. F.; O'Regan, B. C.; Walsh, A.; Islam, M. S. Ionic Transport in Hybrid Lead Iodide Perovskite Solar Cells. *Nat. Commun.* **2015**, *6*, 7497.

(3) Meggiolaro, D.; Motti, S. G.; Mosconi, E.; Barker, A. J.; Ball, J.; Andrea Riccardo Perini, C.; Deschler, F.; Petrozza, A.; De Angelis, F. Iodine Chemistry Determines the Defect Tolerance of Lead-Halide Perovskites. *Energy Environ. Sci.* **2018**, *11*, 702−713.

(4) Kulbak, M.; Cahen, D.; Hodes, G. How Important Is the Organic Part of Lead Halide Perovskite Photovoltaic Cells? Efficient CsPbBr₃ Cells. *J. Phys. Chem. Lett.* **2015**, *6*, 2452−2456.

(5) Yao, Z.; Zhao, W.; Liu, S. F. Stability of the CsPbI₃ perovskite: from fundamentals to improvements. *J. Mater. Chem. A* **2021**, *9*, 11124−11144.

(6) Dastidar, S.; Hawley, C. J.; Dillon, A. D.; Gutierrez-Perez, A. D.; Spanier, J. E.; Fafarman, A. T. Quantitative Phase-Change Thermodynamics and Metastability of Perovskite-Phase Cesium Lead Iodide. *J. Phys. Chem. Lett.* **2017**, *8*, 1278−1282.

(7) Marronnier, A.; Roma, G.; Boyer-Richard, S.; Pedesseau, L.; Jancu, J.-M.; Bonnassieux, Y.; Katan, C.; Stoumpos, C. C.; Kanatzidis, M. G.; Even, J. Anharmonicity and Disorder in the Black Phases of Cesium Lead Iodide Used for Stable Inorganic Perovskite Solar Cells. *ACS Nano* **2018**, *12*, 3477−3486.

(8) Almishal, S. S. I.; Rashwan, O. New accurate molecular dynamics potential function to model the phase transformation of cesium lead triiodide perovskite (CsPbI$_3$). *RSC Adv.* **2020**, *10*, 44503−44511.

(9) Deretzis, I.; Bongiorno, C.; Mannino, G.; Smecca, E.; Sanzaro, S.; Valastro, S.; Fisicaro, G.; La Magna, A.; Alberti, A. Exploring the Structural Competition between the Black and the Yellow Phase of CsPbI$_3$. *Nanomaterials* **2021**, *11*, 1282.

(10) Li, Z.-G.; Zacharias, M.; Zhang, Y.; Wei, F.; Qin, Y.; Yang, Y.-Q.; An, L.-C.; Gao, F.-F.; Li, W.; Even, J.; et al. Origin of Phase Transitions in Inorganic Lead Halide Perovskites: Interplay between Harmonic and Anharmonic Vibrations. *ACS Energy Lett.* **2023**, *8*, 3016−3024.

(11) Yang, R. X.; Tan, L. Z. Understanding size dependence of phase stability and band gap in CsPbI$_3$ perovskite nanocrystals. *J. Chem. Phys.* **2020**, *152*, 034702.

(12) Zhao, B.; Jin, S.-F.; Huang, S.; Liu, N.; Ma, J.-Y.; Xue, D.-J.; Han, Q.; Ding, J.; Ge, Q.-Q.; Feng, Y.; et al. Thermodynamically Stable Orthorhombic γ-CsPbI$_3$ Thin Films for High-Performance Photovoltaics. *J. Am. Chem. Soc.* **2018**, *140*, 11716−11725.

(13) Li, B.; Zhang, Y.; Fu, L.; Yu, T.; Zhou, S.; Zhang, L.; Yin, L. Surface passivation engineering strategy to fully-inorganic cubic CsPbI$_3$ perovskites for high-performance solar cells. *Nat. Commun.* **2018**, *9*, 1076.

(14) Ma, S.; Kim, S. H.; Jeong, B.; Kwon, H.-C.; Yun, S.-C.; Jang, G.; Yang, H.; Park, C.; Lee, D.; Moon, J. Strain-Mediated Phase Stabilization: A New Strategy for Ultrastable α-CsPbI$_3$ Perovskite by Nanoconfined Growth. *Small* **2019**, *15*, 1900219.

(15) Liang, J.; Han, X.; Yang, J.-H.; Zhang, B.; Fang, Q.; Zhang, J.; Ai, Q.; Ogle, M. M.; Terlier, T.; Martí, A. A.; et al. Defect-Engineering-Enabled High-Efficiency All-Inorganic Perovskite Solar Cells. *Adv. Mater.* **2019**, *31*, 1903448.

(16) Ke, F.; Wang, C.; Jia, C.; Wolf, N. R.; Yan, J.; Niu, S.; Devereaux, T. P.; Karunadasa, H. I.; Mao, W. L.; Lin, Y. Preserving a robust CsPbI$_3$ perovskite phase via pressure-directed octahedral tilt. *Nat. Commun.* **2021**, *12*, 461.

(17) Li, F.; Pei, Y.; Xiao, F.; Zeng, T.; Yang, Z.; Xu, J.; Sun, J.; Peng, B.; Liu, M. Tailored dimensionality to regulate the phase stability of inorganic cesium lead iodide perovskites. *Nanoscale* **2018**, *10*, 6318−6322.

(18) Steele, J. A.; Jin, H.; Dovgaliuk, I.; Berger, R. F.; Braeckevelt, T.; Yuan, H.; Martin, C.; Solano, E.; Lejaeghere, K.; Rogge, S. M. J.; et al. Thermal unequilibrium of strained black CsPbI$_3$ thin films. *Science* **2019**, *365*, 679−684.

(19) Akkerman, Q. A.; Meggiolaro, D.; Dang, Z.; De Angelis, F.; Manna, L. Fluorescent Alloy CsPb$_x$Mn$_{1−x}$I$_3$ Perovskite Nanocrystals with High Structural and Optical Stability. *ACS Energy Lett.* **2017**, *2*, 2183−2186.

(20) Protesescu, L.; Yakunin, S.; Kumar, S.; Bär, J.; Bertolotti, F.; Masciocchi, N.; Guagliardi, A.; Grotevent, M.; Shorubalko, I.; Bodnarchuk, M. I.; et al. Dismantling the "Red Wall" of Colloidal Perovskites: Highly Luminescent Formamidinium and Formamidinium−Cesium Lead Iodide Nanocrystals. *ACS Nano* **2017**, *11*, 3119−3134.

(21) Steele, J. A.; Solano, E.; Jin, H.; Prakasam, V.; Braeckevelt, T.; Yuan, H.; Lin, Z.; de Kloe, R.; Wang, Q.; Rogge, S. M. J.; et al. Texture Formation in Polycrystalline Thin Films of All-Inorganic Lead Halide Perovskite. *Adv. Mater.* **2021**, *33*, 2007224.

(22) Goldschmidt, V. M. Krystallbau Und Chemische Zusammensetzung. *Ber. Dtsch. Chem. Ges.* **1927**, *60*, 1263−1296.

(23) Kieslich, G.; Sun, S.; Cheetham, A. K. An Extended Tolerance Factor Approach for Organic−Inorganic Perovskites. *Chem. Sci.* **2015**, *6*, 3430−3433.

(24) Steele, J. A.; Prakasam, V.; Huang, H.; Solano, E.; Chernyshov, D.; Hofkens, J.; Roeffaers, M. B. J. Trojans That Flip the Black Phase: Impurity-Driven Stabilization and Spontaneous Strain Suppression in γ-CsPbI$_3$ Perovskite. *J. Am. Chem. Soc.* **2021**, *143*, 10500−10508.

(25) Straus, D. B.; Guo, S.; Abeykoon, A. M.; Cava, R. J. Understanding the Instability of the Halide Perovskite CsPbI$_3$ through Temperature-Dependent Structural Analysis. *Adv. Mater.* **2020**, *32*, 2001069.

(26) Chen, G.-Y.; Guo, Z.-D.; Gong, X.-G.; Yin, W.-J. Kinetic pathway of γ-to-δ phase transition in CsPbI$_3$. *Chem* **2022**, *8*, 3120−3129.

(27) Steele, J. A.; Braeckevelt, T.; Prakasam, V.; Degutis, G.; Yuan, H.; Jin, H.; Solano, E.; Puech, P.; Basak, S.; Pintor-Monroy, M. I.; et al. An embedded interfacial network stabilizes inorganic CsPbI$_3$ perovskite thin films. *Nat. Commun.* **2022**, *13*, 7513.

(28) Steele, J. A.; Lai, M.; Zhang, Y.; Lin, Z.; Hofkens, J.; Roeffaers, M. B. J.; Yang, P. Phase Transitions and Anion Exchange in All-Inorganic Halide Perovskites. *Acc. Chem. Res.* **2020**, *1*, 3−15.

(29) Lee, C.-H.; Khan, A.; Luo, D.; Santos, T. P.; Shi, C.; Janicek, B. E.; Kang, S.; Zhu, W.; Sobh, N. A.; Schleife, A.; et al. Deep Learning Enabled Strain Mapping of Single-Atom Defects in Two-Dimensional Transition Metal Dichalcogenides with Sub-Picometer Precision. *Nano Lett.* **2020**, *20*, 3369−3377.

(30) Ortiz, B. R.; Peng, H.; Lopez, A.; Parilla, P. A.; Lany, S.; Toberer, E. S. Effect of extended strain fields on point defect phonon scattering in thermoelectric materials. *Phys. Chem. Chem. Phys.* **2015**, *17*, 19410−19423.

(31) Rogge, S. M. J.; Waroquier, M.; Van Speybroeck, V. Unraveling the thermodynamic criteria for size-dependent spontaneous phase separation in soft porous crystals. *Nat. Commun.* **2019**, *10*, 4842.

(32) Rogge, S. M. J.; Borgmans, S.; Van Speybroeck, V. Absorbing stress via molecular crumple zones: Strain engineering flexibility into the rigid UiO-66 material. *Matter* **2023**, *6*, 1435−1462.

(33) Braeckevelt, T.; Goeminne, R.; Vandenhaute, S.; Borgmans, S.; Verstraelen, T.; Steele, J. A.; Roeffaers, M. B. J.; Hofkens, J.; Rogge, S. M. J.; Van Speybroeck, V. Accurately Determining the Phase Transition Temperature of CsPbI$_3$ via Random-Phase Approximation Calculations and Phase-Transferable Machine Learning Potentials. *Chem. Mater.* **2022**, *34*, 8561−8576.

(34) Fransson, E.; Rahm, J. M.; Wiktor, J.; Erhart, P. Revealing the Free Energy Landscape of Halide Perovskites: Metastability and Transition Characters in CsPbBr$_3$ and MAPbI$_3$. *Chem. Mater.* **2023**, *35*, 8229−8238.

(35) Lahnsteiner, J.; Kresse, G.; Heinen, J.; Bokdam, M. Finite-temperature structure of the MAPbI$_3$ perovskite: Comparing density functional approximations and force fields to experiment. *Phys. Rev. Mater.* **2018**, *2*, 073604.

(36) Friederich, P.; Häse, F.; Proppe, J.; Aspuru-Guzik, A. Machine-learned potentials for next-generation matter simulations. *Nat. Mater.* **2021**, *20*, 750−761.

(37) Vandenhaute, S.; Cools-Ceuppens, M.; DeKeyser, S.; Verstraelen, T.; Van Speybroeck, V. Machine learning potentials for metal-organic frameworks using an incremental learning approach. *npj Comput. Mater.* **2023**, *9*, 19.

(38) Jinnouchi, R.; Lahnsteiner, J.; Karsai, F.; Kresse, G.; Bokdam, M. Phase Transitions of Hybrid Perovskites Simulated by Machine-Learning Force Fields Trained on the Fly with Bayesian Inference. *Phys. Rev. Lett.* **2019**, *122*, 225701.

(39) Batzner, S.; Musaelian, A.; Sun, L.; Geiger, M.; Mailoa, J. P.; Kornbluth, M.; Molinari, N.; Smidt, T. E.; Kozinsky, B. E(3)-equivariant graph neural networks for data-efficient and accurate interatomic potentials. *Nat. Commun.* **2022**, *13*, 2453.

(40) Geiger, M.; Smidt, T. M. A.; Miller, B. K.; Boomsma, W.; Dice, B.; Lapchevskyi, K.; Weiler, M.; Tyszkiewicz, M.; Batzner, S.; et al. e3nn/e3nn: 2022-04-13, version 0.5.0; Zenodo, 2022 (accessed Aug 07, 2023).

(41) Sutton, R. J.; Filip, M. R.; Haghighirad, A. A.; Sakai, N.; Wenger, B.; Giustino, F.; Snaith, H. J. Cubic or Orthorhombic? Revealing the Crystal Structure of Metastable Black-Phase CsPbI$_3$ by Theory and Experiment. *ACS Energy Lett.* **2018**, *3*, 1787−1794.

(42) Kühne, T. D.; Iannuzzi, M.; Del Ben, M.; Rybkin, V. V.; Seewald, P.; Stein, F.; Laino, T.; Khaliullin, R. Z.; Schütt, O.; Schiffmann, F.; et al. CP2K: An electronic structure and molecular dynamics software package - Quickstep: Efficient and accurate electronic structure calculations. *J. Chem. Phys.* **2020**, *152*, 194103.

(43) VandeVondele, J.; Krack, M.; Mohamed, F.; Parrinello, M.; Chassaing, T.; Hutter, J. Quickstep: Fast and accurate density functional

calculations using a mixed Gaussian and plane waves approach. *Comput. Phys. Commun.* **2005**, *167*, 103−128.

(44) VandeVondele, J.; Hutter, J. Gaussian basis sets for accurate calculations on molecular systems in gas and condensed phases. *J. Chem. Phys.* **2007**, *127*, 114105.

(45) Goedecker, S.; Teter, M.; Hutter, J. Separable dual-space Gaussian pseudopotentials. *Phys. Rev. B: Condens. Matter Mater. Phys.* **1996**, *54*, 1703−1710.

(46) Perdew, J. P.; Burke, K.; Ernzerhof, M. Generalized Gradient Approximation Made Simple. *Phys. Rev. Lett.* **1996**, *77*, 3865−3868.

(47) Grimme, S.; Antony, J.; Ehrlich, S.; Krieg, H. A consistent and accurate ab initio parametrization of density functional dispersion correction (DFT-D) for the 94 elements H-Pu. *J. Chem. Phys.* **2010**, *132*, 154104.

(48) Grimme, S.; Ehrlich, S.; Goerigk, L. Effect of the damping function in dispersion corrected density functional theory. *J. Comput. Chem.* **2011**, *32*, 1456−1465.

(49) Verstraelen, T.; Vanduyfhuys, L.; Vandenbrande, S.; Rogge, S. M. J. Yaff, yet another force field. http://molmod.ugent.be/softwareweb/ (accessed April 05, 2023).

(50) Hjorth Larsen, A.; Jørgen Mortensen, J.; Blomqvist, J.; Castelli, I. E.; Christensen, R.; Dułak, M.; Friis, J.; Groves, M. N.; Hammer, B.; Hargus, C.; et al. The atomic simulation environment a Python library for working with atoms. *J. Phys.: Condens. Matter* **2017**, *29*, 273002.

(51) Li, Z.; Qin, Y.; Dong, L.; Li, K.; Qiao, Y.; Li, W. Elastic and electronic origins of strain stabilized photovoltaic γ-CsPbI$_3$. *Phys. Chem. Chem. Phys.* **2020**, *22*, 12706−12712.

(52) Teunissen, J. L. *Supporting Data for: "Additivity of Atomic Strain Fields as a Tool to Strain-engineering Phase-stabilized CsPbI$_3$ Perovskites"*; Zenodo, 2023 (accessed March 03, 2023).